

Analyses of Wave Scattering and Absorption Produced by WEC Arrays: Physical/Numerical Experiments and Model Assessment

**H. Tuba Özkan-Haller, Merrick C. Haller, J. Cameron McNatt,
Aaron Porter and Pukha Lenee-Bluhm**

Introduction

The deployment of wave energy converters (WECs) on a commercial scale will necessitate the grouping of devices into arrays to minimize the costs of installation, mooring, maintenance, and electrical cabling for power delivery. The fundamental purpose of WECs is to remove energy from the waves, so they necessarily decrease the wave height in their lee, i.e., they cast a wave shadow. In general, WECs not only capture energy but also redistribute it through the processes of radiation and scattering. The near-field effects of the shadowing and redistribution can have significant implications for the design and performance of WEC arrays (e.g., Beels et al. 2010; Borgarino et al. 2012; Nihous 2012; Babarit 2013; de Andrés et al. 2014; Kara 2016; Sinha et al. 2016). In addition, the far-field effects may extend to the nearshore region (e.g., Millar et al. 2007; Beels et al. 2010; Palha et al. 2010; Smith et al. 2012), where wave-driven currents and sediment transport are the dominant physical processes and are potentially affected by the offshore WEC array

H. Tuba Özkan-Haller (✉)
College of Earth, Ocean, and Atmospheric Sciences, Oregon State University,
Corvallis, USA
e-mail: ozkan@coas.oregonstate.edu

M.C. Haller
School of Civil and Construction Engineering, Oregon State University,
Corvallis, USA

J. Cameron McNatt
Mocean Energy, Edinburgh, UK

A. Porter
Coast and Harbor Engineering, Edmonds, WA, USA

P. Lenee-Bluhm
Columbia Power Technologies, Corvallis, OR, USA

(Rusu and Guedes Soares 2013; Gonzalez-Santamaria et al. 2013; Abanades et al. 2014a and 2014b; Mendoza et al. 2014; O’Dea et al. 2015). Far-field effects may also impact commercial and recreational activities, or ecological processes.

The wave energy industry is still in its nascent stage. Diverse proposed WEC technologies exist, and several field testing sites for wave energy technology have been developed around the world. Comprehensive reviews of WEC technologies can be found in Falcão (2010) and Babarit et al. (2012). Point absorber WECs extract wave energy when wave momentum is transferred to the mechanical motions of the device, which is subsequently converted to other forms of energy. However, the process is not simple—some wave energy is reflected off of the device and additional radiated waves are generated by WEC motion (for reviews of numerical simulation methods, see Li and Yu 2012 and Day et al. 2015). This can lead to a very complex wave field with short-scale variability in the region of the WEC array (e.g., Chatjigeorgiou 2011; Borgarino et al. 2012; McNatt et al. 2013). However, the far field is generally smoothed by the process of wave diffraction and the decay of scattered/radiated waves, and the length scales of variability increase in the far field.

A large number of WEC array studies are performed analytically or computationally. Computational methods are necessary because they underlie the predictive tools used to design WEC arrays and to estimate the nearshore impacts of wave farms at field scales. To gain confidence in these computational tools, they need to be validated with experimental data. To date, only a handful of WEC array experiments have been performed in the laboratory, and WEC array data at the field scale do not yet exist.

Different WEC technologies—including the Salter Duck (Payne et al. 2008), the Manchester Bobber (Alexandre et al. 2009; Weller et al. 2010), the Savonius rotor (Tutar and Veci 2016), oscillating water columns (OWCs; Ashton et al. 2009; Folley and Whittaker 2013; Iturrioz et al. 2014), bottom-pitching WECs (Flocard and Finnigan 2010), and the wave overtopping device WaveCat (Fernandez et al. 2012)—have recently been tested in the laboratory. The study reported here concerns arrays of point absorber WECs (Columbia Power “Manta”); preliminary results were reported by Haller et al. (2011) and Porter et al. (2012).

Much of the previous experimental work was concerned primarily with the energy capture performance of individual WECs and WEC arrays, as opposed to analysis of the wave field changes induced by WEC arrays. Alexandre et al. (2009) presented observations of induced changes in the wave spectrum in the lee of WEC arrays using a set of three wave gages. Their WEC array experiments were at a small scale (1:67) but involved a substantial number of WECs (5×1 and 5×2 arrays) and a single-input Bretschneider wave spectrum. Weller et al. (2010) provided additional data from the same facility with an additional WEC array configuration (3×4). That work focused on WEC power capture and WEC array interaction factors but did not analyze the wave field changes.

Ashton et al. (2009) performed WEC array experiments at a larger scale (1:20) with three different array configurations (1 WEC, 2×1 and 3×2 WEC arrays). They used six wave gages spaced within and around the WEC arrays, and they noted differences between the measured WEC power capture and the wave power deficit measured in the WEC array wave shadow. In fact, in the case of the 3×2 WEC array, a wave power surplus was observed in the downstream wave gage. However, this result is likely an effect of their wave gages being in the near field of the WEC array where the wave field is highly variable at short scales; hence, the wave shadow is much harder to resolve and is not representative of the far-field wave shadow. Ashton et al. (2009) also noted difficulties with analyzing monochromatic wave conditions, again due to high spatial variability. Very recently, Stratigaki et al. (2015) presented a database of laboratory observations of the wave field modification induced by a large 5×5 rectilinear array of heaving WECs (“WECwakes” project).

Finally, field data derived from a single WEC field deployment were published by Eriksson et al. (2007) and Waters et al. (2007, 2011). The deployment involved a floating buoy of 3 m diameter attached to a linear generator and installed at the 25-m depth near Lysekil, Sweden. These data concern device performance as a function of wave conditions.

Here, we report on a comprehensive set of laboratory tests that analyze the near- and far-field modifications due to the presence of an array of five-point absorber WECs. The set of experiments described here is most similar to the set used by Ashton et al. (2009), in that they were performed with WEC arrays of one/three/five devices (here at the 1:33 scale) under both regular monochromatic and fully directional random wave conditions. The key differences in the present work are a significant increase in the available instrumentation for wave observations and a significantly larger suite of tested wave conditions. Further, this work describes two prediction strategies, the phase-resolving model WAMIT (see WAMIT, Inc. 2000) and the phase-averaged Simulating WAVes Nearshore (SWAN) model (Booij et al. 1999), and compares them to the wave observations. Results reveal the fidelity of each model and help to frame their appropriate future implementation and uses for WEC array modeling. Additionally, the experimental and model data contribute to the description of the WEC-induced wave field and inform effective WEC array design.

This chapter begins with a review of the laboratory experiments (section “[WEC Array Laboratory Experiments](#)”), including details about the wave conditions, WEC devices, instrumentation, and observational strategies for the determination of absorbed wave power. In section “[Numerical Modeling](#),” we discuss the two wave modeling strategies, giving special attention to the wave power extraction formulations. Model results and comparisons to wave observations are given in section “[Results](#).” In section “[Discussion](#),” we discuss further model simulations and their implications for the SWAN model WEC formulation with regard to the capability of simulating wave shadows induced by WEC arrays.

WEC Array Laboratory Experiments

Laboratory experiments were conducted at Oregon State University (OSU) in collaboration with Columbia Power Technologies, Inc. (CPT). The experiments were conducted in the Hinsdale Wave Research Laboratory, used 1:33 scale versions of the CPT “Manta” device (version 3.1), and included an extensive matrix of incident wave conditions and WEC array configurations. Array configurations of one, three, and five devices were moored inside the Tsunami Wave Basin (TWB), and incident wave conditions consisted of a range of regular monochromatic and random spectral sea states. Many of the spectral sea states also included directional spreading.

The TWB is 48.8 m long and 26.5 m wide. It has a directional wavemaker consisting 29.2 m wide, piston-type wave paddles that are individually controlled. During the experiments, a crushed rock beach (1:12 slope) was installed opposite the wavemaker for wave dissipation, and the still water depth was maintained at 1.37 m on average.

Incident Wave Conditions

Experimental wave conditions included normally incident and oblique regular waves and long- and short-crested irregular waves. The laboratory-scale wave heights and periods were devised from targeted field-scale conditions and Froude scaling. The field-scale monochromatic wave periods ranged from 5.2 to 16 s (laboratory scale 0.9–2.8 s) and field-scale heights from 1 to 5 m (laboratory scale 3–15 cm). Most wave conditions were normally incident (with respect to the wavemaker as well as the WECs), but a limited set of regular monochromatic wave conditions was generated at 22.5 degrees incidence. Table 1 summarizes all of the tested regular wave conditions. This analysis focuses on the field-scale wave heights of 2 m (6 cm) because those runs contain the widest variety of wave periods and WEC array configurations. Most of the regular wave trials contained 50 waves. However, early in the experiment, some wave tests were conducted with only 12 waves.

Irregular wave conditions were intended to simulate sea state climatology at different potential WEC array installation sites. Seven target sea states were chosen and are listed in Table 1 (lower portion). They consist of five Oregon sea states (Oregon 1–5) ranked in the order of increasing wave power and a target Hawaii and Ireland sea state. The five Oregon sea states roughly span the climatology observed in 13 years of wave data derived from National Data Buoy Center Station 46050 (NDBC Stonewall Banks). The Hawaiian sea state is at a relatively shorter wave period and was derived from NDBC 51202. The Ireland sea state is of relatively higher energy and was derived from the M4 buoy. The Oregon storm conditions were derived from a peak-over-threshold extreme wave analysis of the NDBC

Table 1 Experimental wave conditions (top panel). Regular wave conditions, all cases include both incident angles 0° and 22.5° except for “T = 6 (o)” which is oblique 22.5° only. Values in the table indicate the number of WECs (1, 3, or 5) (bottom panel). Laboratory-scale conditions for random sea states. 2* indicates a case tested only with 3 and 5 WEC configurations. UD indicates unidirectional cases; s refers to the directional spreading parameter

| Regular waves—wave period (s) | | | | | | | | | | | | | | | | | | | | | |
|-------------------------------|---------|---------------|---------|------------------|---------|-----------------------|---------|----------------------|---------|-----------|---------|---------|---------|---------|---------|---------|---------|---------|---------|---------|---------|
| H (cm) | T (sec) | 0.9 | 1.0 | 1.1 | 1.2 | 1.3 | 1.4 | 1.5 | 1.6 | 1.7 | 1.8 | 1.9 | 2.0 | 2.1 | 2.2 | 2.3 | 2.4 | 2.5 | 2.6 | 2.7 | 2.8 |
| | 3 | | 1 | | 1 | | 1 | | 1 | | 1 | | 1 | | 1 | | 1 | | 1 | | 1 |
| | 6 | 1, 3, 5 | 1, 3, 5 | 1, 3, 5 | 1, 3, 5 | 1, 3, 5 | 1, 3, 5 | 1, 3, 5 | 1, 3, 5 | 1, 3, 5 | 1, 3, 5 | 1, 3, 5 | 1, 3, 5 | 1, 3, 5 | 1, 3, 5 | 1, 3, 5 | 1, 3, 5 | 1, 3, 5 | 1, 3, 5 | 1, 3, 5 | 1, 3, 5 |
| | 6(o) | | | | | | | | | | 3,5 | | | | 3,5 | | | | | | 3,5 |
| | 9 | | 1, 3, 5 | | 1, 3, 5 | 1, 3, 5 | 1, 3, 5 | | 1, 3, 5 | | | | 1, 3, 5 | | | | | | 1, 3, 5 | | |
| | 12 | | | | | 1, 3, 5 | 1, 3, 5 | | 1, 3, 5 | | | | 1, 3, 5 | | | | | | 1, 3, 5 | | |
| | 15 | | | | | 1, 3, 5 | 1, 3, 5 | | 1, 3, 5 | | | | 1, 3, 5 | | | | | | 1, 3, 5 | | |
| Real seas target conditions | | | | | | | | | | | | | | | | | | | | | |
| Wave height | | Peak period | | Peak direction | | Directional spreading | | Sea state | | WEC ARRAY | | | | | | | | | | | |
| H_{msl} (cm) | | T_p (sec) | | θ_p° | | s^l | | | | | | | | | | | | | | | |
| 4.5 | | 1.2, 1.6 | | 0, 22.5 | | 2*, 4, 10, UD | | HI—Kaneohe, Oregon 1 | | 1, 3, 5 | | | | | | | | | | | |
| 7.6 | | 1.4, 1.8, 2.2 | | 0, 22.5 | | 2*, 4, 10, UD | | Oregon 2, 3, 4 | | 1, 3, 5 | | | | | | | | | | | |
| 10.6 | | 1.6 | | 0, 22.5 | | 2*, 4, 10, UD | | IR—M4 Buoy | | 1, 3, 5 | | | | | | | | | | | |
| 13.6 | | 2.2 | | 0, 22.5 | | 2*, 4, 10, UD | | Oregon 5 | | 1, 3, 5 | | | | | | | | | | | |
| 30 | | 2.6 | | 0 | | UD | | Oregon storm | | 1 | | | | | | | | | | | |
| 45.2 | | 2.6 | | 0 | | 2, UD | | 100-yr storm | | 1 | | | | | | | | | | | |
| 45.2 | | 2.6 | | 22.5 | | UD | | 100-yr storm | | 1 | | | | | | | | | | | |

46050 data. Note that in this chapter, we only analyze a subset of these sea states, but they are all listed here for completeness. The generated wave frequency spectrum used the Pierson–Moskowitz model with a range of different directional spreading factors representative of the NDBC 46050 data. The irregular wave run-times ranged from 313 to 540 s, which was longer than the run-times of regular waves in order to improve the statistical significance of the collected data.

Model WECs and WEC Arrays

Five experimental WECs were fabricated for the experiments. They were designed as scaled versions of the Columbia Power Manta 3.1, and each consists of three rigid bodies as shown in Fig. 1. The central body is composed of the main spar and a nacelle, and is designed to stay relatively stationary in heave due to the large damper tank at its base. Two identical fore and aft floats differ by a rotation of 90° , as attached. The fore and aft floats are free to move only in pitch with respect to the central body. Thus, the WECs are constrained to move in a total of eight degrees of freedom (DOF), one for each float (relative pitch) and six for the central body (surge, sway, heave, roll, pitch, and yaw).

Each float is connected to the top of the spar through a drive shaft, and model generators are actuated by the relative motion between each float and the spar. The

Fig. 1 Manta 3.1 WEC assembly



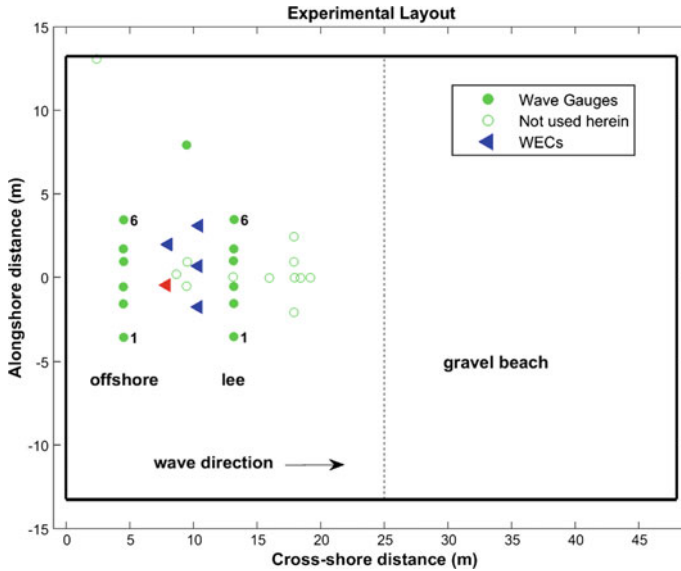


Fig. 2 Location of offshore and lee wave gage arrays (*filled green circles*), location of WECs for the single WEC experiments (*red triangle*), and locations of the 5-WEC experiments (combination of *red and blue triangles*)

generators were modeled using oil-filled rotary dashpots that were calibrated before deployment. A linear damping estimate was calculated via a least squares linear fit of measured torque to speed. Damping estimates for each dashpot were performed both pre- and post-experiment and were found to have changed significantly. Torque (the product of damping and rotational velocity) was not measured during the experiments, so for the power capture analysis the damping coefficients were assumed to trend linearly between the pre- and post-experiment values.

Three WEC configurations were tested—a single WEC and arrays of three and five WECs. The WEC arrangements are shown in Fig. 2. The mooring of each WEC was accomplished by running horizontal elastic lines between vertical stanchions and the damper tank of each WEC in a symmetrical three-point configuration. The elastic lines were selected to have a load/displacement curve that was similar to the field-scale mooring system design. At the laboratory scale, the WECs have a beam of 0.55 m (18 m at prototype) and the draft from the surface to its lowest point is 0.75 m.

Wave Instrumentation

The extensive set of instrumentation used during the experiments included 28 in situ instruments (wave gages and current meters) arranged in small arrays

designed to resolve the wave field offshore of the WEC array as well as in the immediate lee and far field of the WEC array. In addition, three acoustic Doppler velocimeters with co-located wave gages were arranged within the WEC array to capture near-field wave information. Because the near-field wave patterns were expected to be highly variable and difficult to measure in situ, a bi-static camera system was installed on the ceiling to attempt three-dimensional wave imaging through binocular stereovision techniques. Initial results from the analysis of those data are provided by Black and Haller (2013); here, we focus only on the observations offshore and in the lee of the WEC arrays. A schematic of the TWB coordinate system and the instrument and WEC locations is shown in Fig. 2. Wave gages were sampled at 50 Hz. More information about the experimental design and analysis procedures can be found in Rhinefrank et al. (2013).

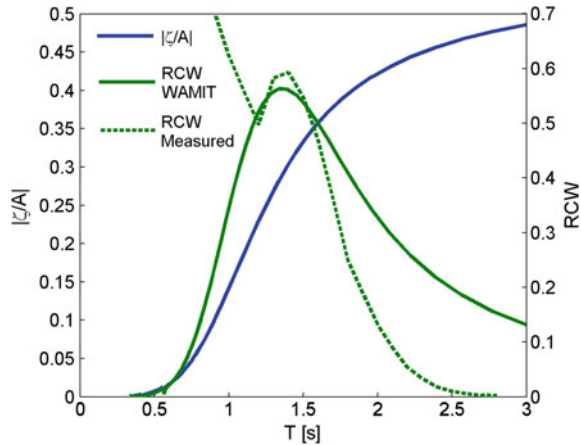
Determination of the Relative Capture Width

A commercial motion-tracking system was installed on each of the WECs, and the motion data for the three rigid bodies composing each WEC (8 DOF) were used to estimate power capture. The system used a swarm (~90 total) of light-emitting diodes (LEDs) attached to lightweight rods on each of the three bodies composing the individual WECs. These active LEDs were tracked with a network of cameras installed on a frame above the tank. During wave action, the system of markers and cameras allowed the motion of each rigid body component to be tracked at 480 Hz. Subsequently, a zero-phase low-pass filter (50 Hz) was applied to the motion data, and the resulting signals were down-sampled to 50 Hz for analysis.

The velocity of the relative rotation of each float with respect to the spar, referred to as the generator speed, is needed to estimate the absorbed mechanical power; it was determined by differencing the relative rotation position signal and dividing by the 50 Hz time step. The signals were not de-trended for this calculation. The instantaneous mechanical power is calculated for each generator (fore and aft) as the product of the generator speed and the torque. The generator torque is calculated as the product of the estimated linear damping coefficient of the characterized generator and generator speed signal. The mean mechanical power of the fore and aft generators sum to the mean mechanical power of the total system. This procedure is used to calculate mean mechanical power in regular waves and real seas.

WEC performance is quantified as the mean mechanical power, normalized by the mean wave power incident across a width equal to the nominal WEC width (54.54 cm). This dimensionless performance parameter, used extensively in the WEC industry, is called the relative capture width (RCW) and can be thought of as the proportion of incident wave energy (in a crest length equal to the nominal WEC dimension) captured by the device. The power absorption characteristics of the experimental WEC were measured at individual frequencies across a range of regular wave conditions using the motion capture data. The resulting measured RCW is shown as the dashed line in Fig. 3. Data only exist for wave periods

Fig. 3 Modeled WEC surge motion (*solid blue*) and the measured (*dashed green*) and WAMIT modeled (*solid green*) power absorption plotted versus wave period. The power absorption is plotted as the relative capture width (RCW), which is the ratio of the power absorbed by the device to the wave energy flux incident to its width



ranging from 0.9 to 2.7 s because they represent the extent of regular wave testing. The experimentally determined RCW curve demonstrates a peak near 1.4 s, and no power is absorbed for waves with periods longer than about 2 s. Additional analysis (not shown here) has extended the experimentally measured RCW to wave periods shorter than 0.9 s (see Rhinefrank et al. 2013). The extended experimental curve indicates increased RCW at even shorter wave periods. However, the extended RCW information has limited impact on the conditions analyzed here (see Table 1), which are composed of regular wave cases with the specific range of periods described by the RCW curve in Fig. 3 (0.9–2.7 s) and real sea state conditions that contain little or no energy at periods shorter than 0.9 s.

Numerical Modeling

When waves encounter WECs, portions of their energy are absorbed or scattered. A shadow region forms behind the devices but the diffraction process, acting over long distances shoreward, reduces the wave shadow by transmitting energy into the lee of the array. As a result, the wave field is modified both offshore of the array as well as in its lee. If the WECs are mobile in at least one degree of freedom (which most point absorber WECs are designed to be), the wave forces induce WEC motion, which generates additional wave motions (see Mei 2012 for a review). The feedback between the wave field and the WECs can, therefore, be quite complex, and the resulting combined wave field typically displays complex partial standing wave patterns. Such patterns also occur when a wave field interacts with isolated bathymetric features (for example, see Choi et al. 2009), and their prediction requires the consideration of wave-phase information. The partial standing wave patterns are known to be most pronounced for regular wave conditions and can be best captured using phase-resolving wave models. In contrast for random wave

conditions with directional spreading, the patterns are much less pronounced, and phase-averaged models can successfully predict the overall wave field (Choi et al. 2009).

To date, several types of models have been used to simulate wave–WEC interactions. The models range in complexity and vary in their ability to account for wave-phase information. In this chapter, we evaluate the performance of two such models. Specifically, we compare the performance of a phase-resolving and a phase-averaged model (WAMIT and SWAN, respectively) in the simulation of the experimental conditions. In addition, we use the phase-resolving model to analyze the impact of incident wave frequency on wave scattering and radiation from an individual WEC, and assess the applicability of either model for the variety of experimental wave conditions considered.

Phase-Resolved Linear Wave Theory—WAMIT

WAMIT is a state-of-the-art commercial boundary-element solver (WAMIT, Inc. 2000) that simulates linear hydrodynamic forces on immersed objects due to planar waves. It solves the standard linear wave-body boundary-value problem in the frequency domain. The assumptions underlying the model are that (1) the fluid is incompressible and inviscid; (2) the flow is irrotational and the velocity can be expressed as the gradient of a scalar velocity potential; (3) the wave height is small compared to the wavelength and water depth; and (4) the amplitudes of body motions are small compared to the size of the body. The latter two assumptions enable the use of linear wave (airy) theory. To find the solution to the boundary-value problem, WAMIT uses the boundary-element method, in which all body surfaces are represented as source or dipole functions that satisfy the governing equation (Laplace’s equation for the velocity potential) and the free surface condition; the magnitudes of the dipole functions satisfy the no-penetration condition on all wetted surfaces.

Because WAMIT assumes linear waves, each frequency component can be treated independently and the velocity potential associated with each frequency component can be summed to describe the total fluid motion. All other variables of interest (i.e., flow velocities, surface elevation, and pressure fields) can be computed using the velocity potential and well-known linear wave theory formulations. Also, thanks to the assumption of linearity, the total velocity potential at a given frequency can be found as the superposition of the incident and scattered velocity potentials (ϕ_i and ϕ_s , respectively) and the radiation velocity potentials (ϕ_r^j) due to body motions in each degree of freedom, j . The scattered potential is the modification of the wave field due to the encounter with the device. The sum of the incident and scattered potentials is often referred to as the diffraction wave potential. The pressure field on the structure associated with the combination of the incident and scattered wave potentials is used to estimate the motion of the device,

and this motion results in the generation of radiated waves, described by the radiation velocity potentials, ϕ_r^j , associated with each degree of freedom of the device.

Spectral wave fields are considered by evaluating multiple wave components at given frequencies (ω) and directions (β), and associating an amplitude with the incident wave component as defined by an incident wave spectrum, $S_i(\omega, \beta)$. At a given frequency and direction, the magnitude of the incident wave amplitude is $|A| = \sqrt{2S_i(\omega, \beta)\Delta\omega\Delta\beta}$, where $\Delta\omega$ and $\Delta\beta$ are the bin widths at the given frequency and direction, respectively. For the phase of the incident wave components, random values are chosen from a uniform distribution between 0 and 2π . From the point spectrum, the bulk parameter of the zeroth-moment significant wave height can be computed as $H_s = 4\sqrt{\sum \sum S(\omega, \beta)\Delta\omega\Delta\beta}$.

To model the WEC array experiments described above, a geometric model of the physical WEC being tested is required. As an initial assessment, a simple cylinder was adopted as the geometry for the computational model. Although a cylinder is a very rough approximation of the physical model, the behavior of the cylinder can be controlled to closely mimic the WEC. First, the dimensions of the cylinder were chosen to match the approximate size of the physical model; the diameter of the cylinder is 0.6 m and the draft is 0.8 m. Second, the single degree-of-freedom mode of motion was chosen to be surge, because the surge motion of the cylinder most closely resembles the power-absorbing motion of the physical model WEC under consideration. In particular, the power absorption curve of the surging cylindrical WEC reproduces the important portions of the power absorption curve associated with the physical model WEC (see Fig. 3 for the comparison). Finally, a power take-off (PTO) damping for the computational model WEC was chosen (at 2000 kg/s), so that the peak absorbed power was of the same approximate magnitude and occurred at approximately the same frequency as in the physical model (Fig. 3).

The modeled wave field domain is the same size as the TWB. The water depth was fixed at 1.4 m throughout the domain. No effort was made to model the sloping beach, wave basin walls, or the wavemaker. Wave data from 21 wave gages are available for comparison. Comparisons are made directly at two sets of wave gages. The offshore set corresponds to the set of six gages that were between the WEC arrays and the wavemaker. The set of lee instruments corresponds to a line of six gages behind the WECs. The offshore and lee wave gages are numbered 1–6 from left to right facing the wavemaker. The wave gage and WEC positions are shown in Fig. 2.

Phase-Averaged Linear Wave Theory—SWAN

The SWAN model was designed to simulate the transformation of the wave action density spectrum over a variable bathymetry and ambient current field, as well as

the energy gain or loss of wave components due to mechanisms such as wind input and wave dissipation (Booij et al. 1999). Like WAMIT, SWAN is essentially based on linear wave theory; hence, a spectral sea can be represented as the sum of harmonic wave components at given frequencies and directions (although some empirical formulations can be included to account for nonlinear processes such as wave–wave interactions). In SWAN, all wave components are planar, and the wave action density of each wave component is considered through a conservation of action equation solved over a regular grid using finite difference methods (an unstructured grid option also exists; see Zijlema 2010). For the computation of wave action density, the relevant quantities are the magnitude of the planar wave component, or wave height, and its relative frequency and direction; the phase of the wave component is not considered.

The SWAN model has an option to include the representation of coastal structures, such as breakwaters or jetties (Ilic et al. 2007). However, in this standard option the structures are represented relatively simplistically using frequency-independent modifications of the wave action spectrum via reflection and transmission coefficients that must be pre-determined for the given structures. Further, the absence of wave-phase information precludes SWAN from providing a more realistic representation of the effect of immersed bodies on the wave field, because the reproduction of conditions with intersecting wave trains (that form partial standing wave patterns) would require knowledge of phase information associated with the wave components.

In this work, we are interested in improving the representation of immersed bodies in the SWAN model and implementing a representation of the WEC structure that includes information about the frequency-dependent nature of the energy absorption. This is achieved by using a nested-domain approach. For a situation involving multiple rows of WEC devices, the nested approach involves dividing the domain into multiple adjacent sub-domains separated by rows of WECs. SWAN is then used to propagate waves from the offshore boundary through the first sub-domain to the first row of WECs. The SWAN-produced wave spectra at the locations of the WECs are then manually altered given the experimentally determined, frequency-dependent RCW (Rhinefrank et al. 2013) associated with each WEC. The resulting alongshore-variable wave field then enters the next shoreward sub-domain, and the evolution of this wave field is computed using SWAN until the next row of devices is encountered. Similar frequency-dependent WEC formulations for spectral wave models were given by Alexandre et al. (2009) and Silverthorne and Folley (2013); however, they used theoretical RCW curves with limited (if any) comparisons to field observations. Chang et al. (2016) have incorporated the methodology we used here into the SWAN source code, which eliminates the need for nesting and external modification of the spectra.

Even though our implementation is an improvement over many preexisting representations of WECs in the SWAN model, it has several important shortcomings. In particular, wave field effects are accounted for only in the lee of the devices and are the result of only WEC power absorption. Hence, the implementation does not consider any scattered or radiated wave energy. Furthermore, no modification to

the wave direction in the shadow region is produced. Use of the diffraction formulation included in the SWAN model (Holthuijsen et al. 2003) can potentially remedy this latter shortcoming, but, given the phase-averaged nature of SWAN, this formulation only reproduces the modification to the group velocity associated with wave components and will still not produce a realistic phase-dependent diffraction pattern. Use of the diffraction formulation also comes at a significant computational cost that can lead to difficulties in achieving a desired spatial resolution. Despite these shortcomings, ascertaining the conditions under which this approximate treatment in SWAN is adequate to obtain a reasonable representation of the near-field wave field is of interest.

To model the experiments, the entire TWB is considered using the measured basin bathymetry (obtained using a mobile lidar system). Monochromatic wave cases are approximated with a very narrow spectral shape. To assess the model skill at reproducing the observed conditions, we consider a metric that is indicative of the overall reduction in wave power in the lee of the WECs. We define this power loss metric by considering the difference between the incident wave energy flux through an alongshore transect and the net wave energy flux integrated over the same alongshore distance in the lee of the WECs. The total alongshore distance considered for the power loss metric is the extent of the alongshore array of gages (see Fig. 2). For spectral sea comparisons, the energy flux computation requires integrating over frequency and direction.

Results

The results section is divided into two parts: In the first part, in order to elucidate the spatial scales of scattering and radiation induced by WECs and their dependence on incident wave frequency, WAMIT wave fields are compared to the experimental observations. This comparison also assesses the ability of the WAMIT model setup to simulate the overall experimental conditions. In the second part, the magnitude of the wave shadow simulated by the SWAN model with the experimentally determined RCW is compared to the wave shadow observations.

WAMIT-Data Comparisons

We begin our analysis with the cases involving 1 or 5 WECs subjected to regular wave conditions (Fig. 4) and spectral sea states (Fig. 5). To quantify the importance of the wave field changes induced by the WEC arrays, the observed wave heights are normalized by the measured incident wave height for each case. It should be noted that defining/measuring the incident wave height with the laboratory data introduces challenges due to the near-immediate presence of WEC-scattered waves offshore of the WECs. Here, for the incident wave height we take the average of all

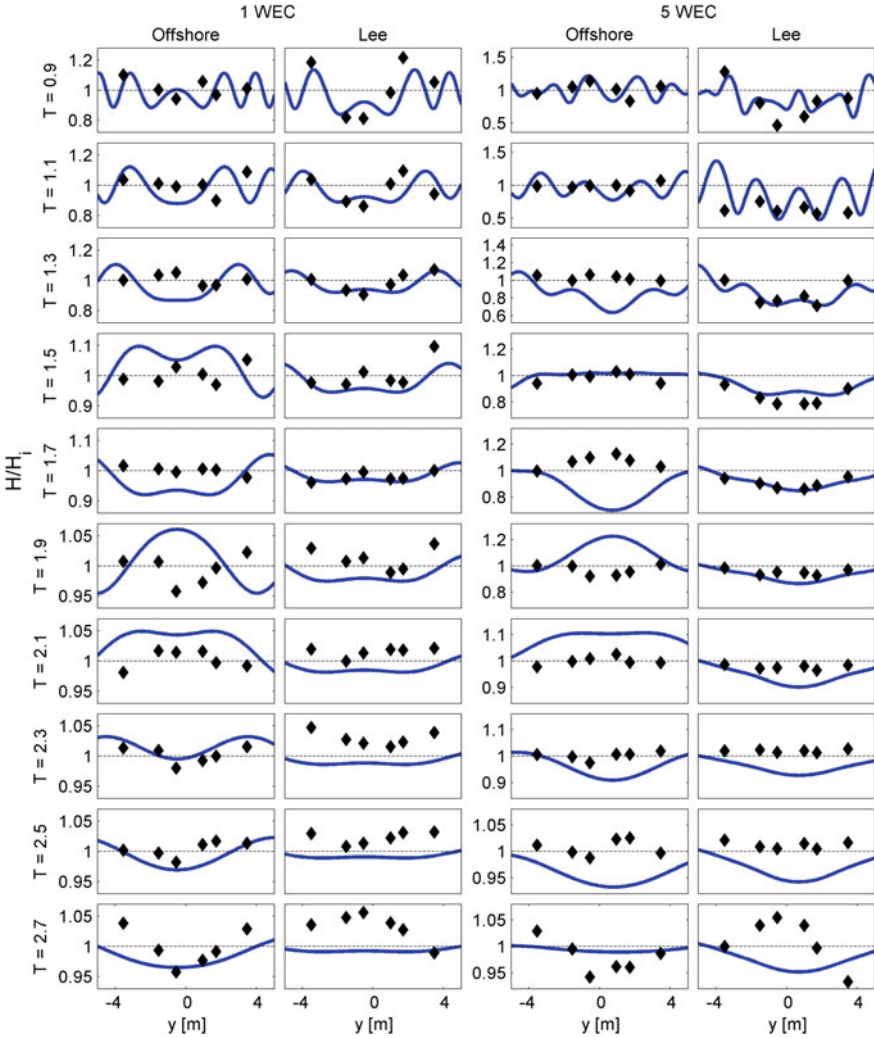


Fig. 4 WAMIT model results (*lines*) and observations (*black diamonds*) for the regular wave cases with 1 WEC (*columns 1 and 2*), and 5 WECs (*columns 3 and 4*). For each WEC array, the *left column* shows offshore data and the *right column* the lee data. Wave heights normalized by the average incident wave height (H/H_i) for different wave periods as indicated on the left-hand side of each row

of the wave height measurements at the offshore gage array, including the lone gage positioned at $\sim [9, 8 \text{ m}]$ (cross-shore, alongshore) about 5 m alongshore from the WEC array.

For the conditions involving wave periods of 0.9 and 1.1 s, the WAMIT results demonstrate that the near-field waves are highly variable spatially and are consistent

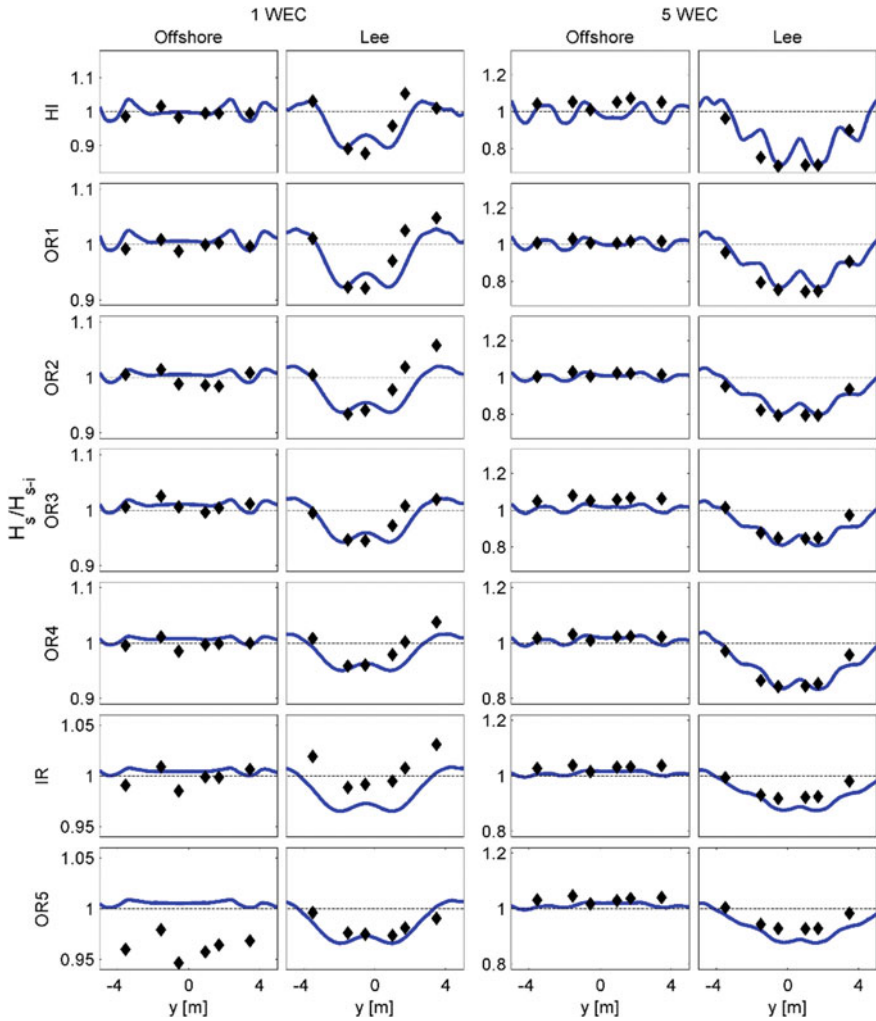


Fig. 5 Same as Fig. 4 but for spectral sea states. Sea states listed at the far left

with the well-known alongshore standing wave ridge pattern (see also Farley 2011 and McNatt et al. 2013). For these periods, the length scales of variability are short (~1 m) and the amplitude variability is relatively large ($\pm 20\%$ change from incident wave height for 1 WEC and close to 50% for the 5 WEC cases), and multiple ridges are present within the observational arrays.

The full spatial standing wave ridge patterns simulated by WAMIT for the 1 WEC cases are also shown in Fig. 6 (left panels), in which the short-length scales of the wave height variation are very evident, especially for the shortest wave periods. The results show that the amplitude of the wave height ridge pattern is more

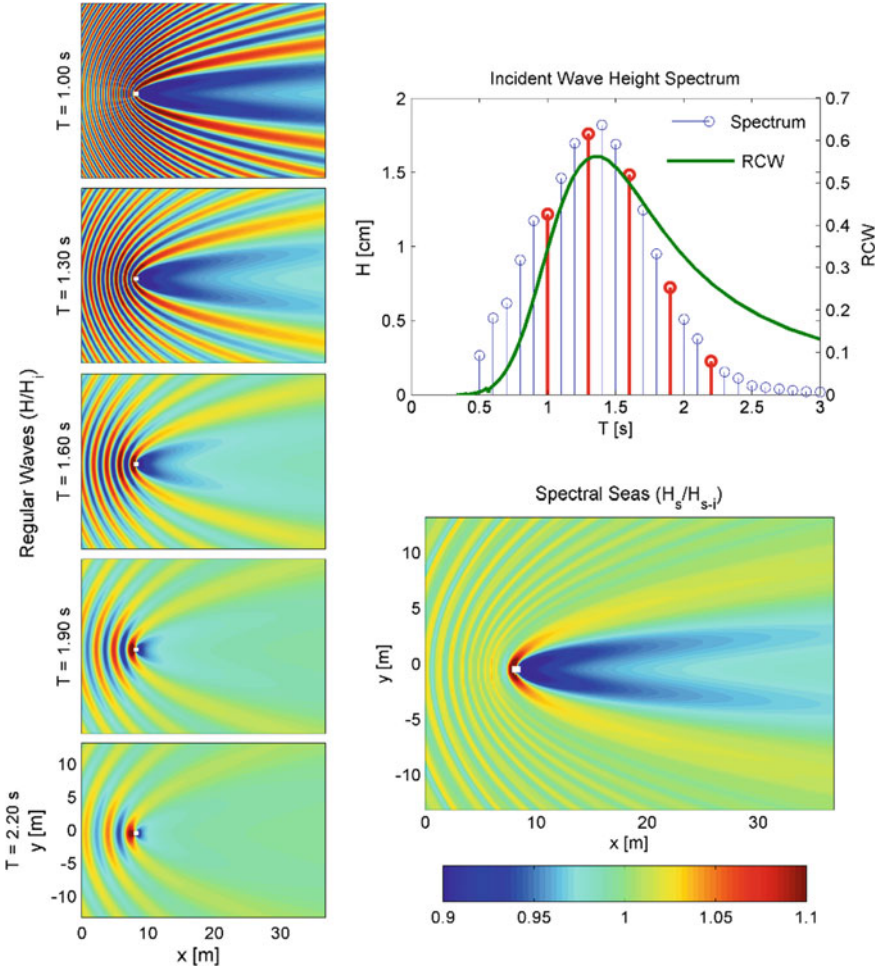


Fig. 6 (Left panels) Wave height modification (local wave height normalized by incident wave height) for different wave components (top-right panel) wave heights of individual components of the spectrum (left panels correspond to red components) with the modeled RCW curve, and (bottom-right panel) normalized significant wave height including all components ($T_p = 1.4$ s)

pronounced for short periods, which indicates that the reflected and radiated wave components are more important for short-period waves than for long-period waves. This is consistent with the device motion estimates produced by WAMIT (see Fig. 3), which indicate that the WEC functions as a wave follower (i.e., motion amplitude is more similar to the incident wave amplitude and phase coupling with the incident waves) for large periods (i.e., periods \geq peak RCW). Hence, shorter incident waves are associated with more energetic radiated wave components. One ramification of the related redistribution of wave energy is that the shadow region is more pronounced for short-period waves.

The short-scale variability under regular wave conditions is clearly evident in the laboratory observations (Fig. 4). Of course, the observed ridge locations must have some sensitivities to the details of the WEC shape and response characteristics as well as to the finite drift of the WECs on their compliant moorings; hence, the partial standing wave pattern likely has some additional space/time variabilities beyond the WAMIT modeling capabilities as we have it configured here. Despite these shortcomings, the locations of the peaks and troughs of the ridges, as well as the magnitude of the wave height variability in the regular wave cases, are fairly well simulated by WAMIT. The short-scale variability is present in both of the alongshore arrays, in the lee as well as offshore of the WECs. The lee transect primarily demonstrates the wave shadow and an overall reduction in wave height directly behind the devices and provides evidence of corresponding ridges at alongshore distances from the edge of the WEC arrays (e.g., $T = 0.9$ s, 1/5 WEC lee array). The offshore data also show the effects of the scattering of wave energy from the WECs as well as the radiated waves due to WEC movement. The amplitude of wave height variability in the offshore array significantly decreases with wave period. The model results provide much-needed context for the observations given that the observations only sparsely sample the short-scale variability of the wave pattern.

The trend in the spatial structure in the lee of the WECs is that it smooths out (i.e., the spatial scales increase) for cases with longer wave periods and more resembles a simple wave shadow for which the wave height deficit signal also decreases for periods greater than 1.5 s. The results for the 1.3, 1.5, and 1.7 s periods show very good agreement (especially at the lee transect), but the measured transect is not wide enough to capture a full-standing wave pattern. The magnitude of the wave modification is not large, $\pm 10\%$, for these cases. For even longer periods, the wave height modification at the lee transect is minimal ($< 5\%$, note the scale changes in the plots), and the length scales are large enough where no major oscillations are expected within the observational transect. The model/data disagreement appears to be larger for the longer wave periods, but it should be considered in the context of the small signal-to-noise ratio as wave period increases, the experimental uncertainties, and the necessary model approximations. In addition, the relative distance (distance divided by wavelength) between the WEC arrays and the lee transect is greater for the shorter waves, which may make the results somewhat less dependent on the details of the WEC geometry or the translation and movement of the individual WECs.

On the other hand, the general realism shown by the model data comparisons can be attributed to the accurate geometric size of the model WECs and their reasonable approximation of the power capture characteristics of the physical devices even though they are represented rather simplistically as moving cylinders. In general, it appears that phase-resolved, linear wave theory has some skills in modeling the wave field for both single and multiple WEC configurations, and that the predicted standing waves do indeed exist. Note that the correct interpretation of the peaks and troughs of the data transect would have been very difficult without having the phase-resolved computational model for context.

In spectral seas, the computational prediction and experimental data match well (Fig. 5) for both the 1-WEC and 5-WEC cases. Figure 6 (left panels and bottom-right panel) also illustrates the contributions of individual frequency components to the overall wave height variation for spectral seas. In the figure, the modifications to the wave field due to specific frequency components are shown along with the total resultant significant wave height spatial variability when the entire spectrum is considered (spectral peak at $T = 1.4$ s, top-right panel). Both figures demonstrate that, at the offshore gage array, the significant wave height is fairly uniform, and in the lee of the devices the structure of the wave shadow is fairly consistent for all sea states. The wave shadow is easily discerned in the both model and data, and the model appears to accurately capture the alongshore scale and magnitude. A few cases appear to show a vertical offset but an appropriate alongshore trend. We attribute this to the small signal-to-noise ratio of the wave shadow we have tried to capture here (wave height differences of the order 2–3% in some cases).

The spatial variation in wave height due to standing waves that is quite pronounced in the regular wave cases is smoothed when random waves are considered. This is because the wave components of differing frequencies that make up the random wave field are associated with standing wave ridge patterns with nodes that occur at differing locations. The significant wave height (shown in Figs. 5 and 6 bottom-right panel) is indicative of a composite of the spatial patterns associated with the individual wave components and therefore displays much less variability in space. This is especially evident at the offshore observational transect. At the lee transect, a wave shadow pattern exists in addition to the short-scale variability due to the standing wave ridge pattern. Although the locations of the nodes associated with the ridge patterns all vary with frequency at the lee transect, the wave shadows at different frequencies occur at mostly the same locations. As a consequence, the wave shadow effect is more pronounced for the random wave cases.

SWAN Data Comparisons

The SWAN simulations approximate only the formation of the shadow in the lee of the devices and cannot capture the nodal structure associated with the standing wave ridge pattern. This is primarily because of the phase-averaged nature of the model; hence, radiated waves are not simulated; only the extraction of wave energy due to the WECs and the associated reduction in the wave action density spectrum are considered. Therefore, we evaluate the ability of the SWAN simulations to reproduce the bulk description of the wave shadowing when a realistic device RCW curve is used. The wave shadow estimated by the model is taken as the net power deficit between the offshore and lee array locations as evidenced in the SWAN simulations. Because the wave propagation distance between the WECs and the lee array is short, this deficit is mostly (but not entirely) determined by the model spectral modifications applied at the WEC locations, which are directly determined

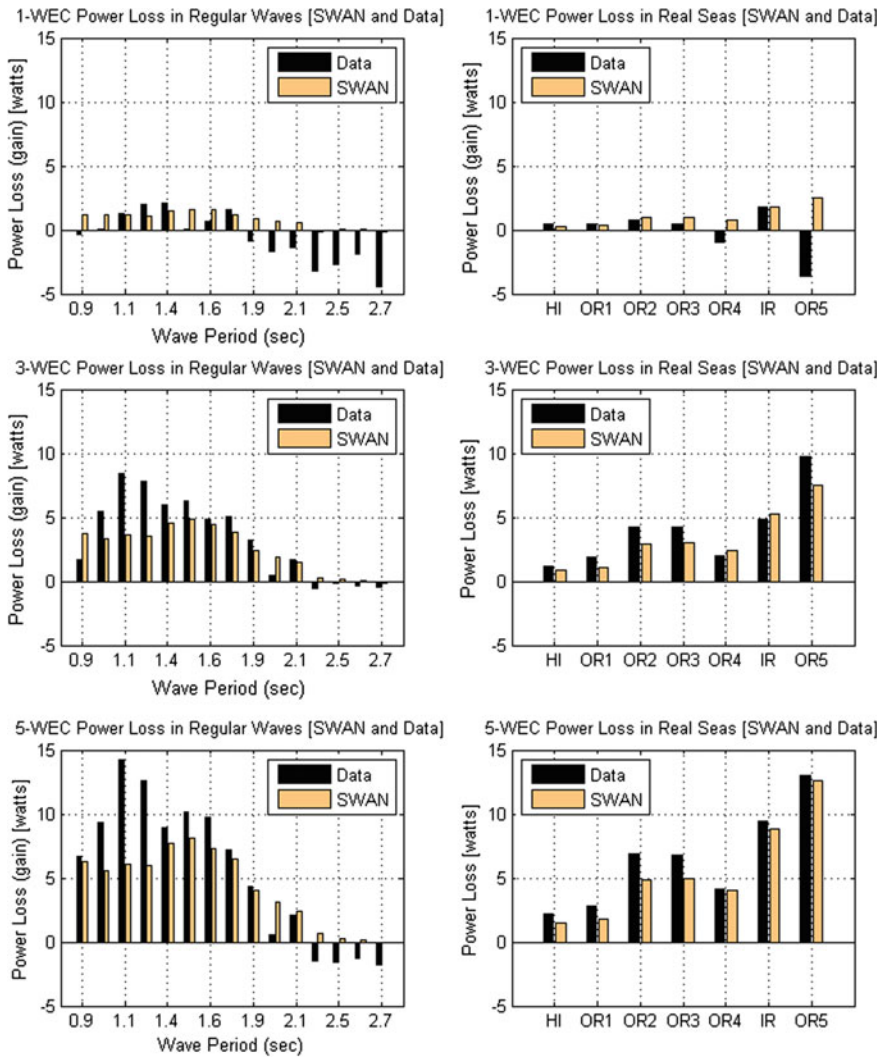


Fig. 7 Wave energy flux deficit measured by gage arrays (*black bars*) and SWAN-simulated (*tan bars*). Deficit is defined as the difference between the wave energy flux offshore and in the lee of the devices for 1-WEC (*top row*), 3-WEC (*middle row*), and 5-WEC (*bottom row*) arrays for regular wave cases (*left column*) and real sea states (*right column*)

from the experimental RCW curve developed from the WEC motion observations. In Fig. 7, the wave shadow estimated in the model is compared to the net difference between the observed wave energy flux crossing the offshore gage array and that crossing the lee wave gage array.

Immediately evident from Fig. 7 is that the SWAN data comparisons for real sea states (right column) are generally quite good. Also evident for both regular waves

and real seas (both columns) is the relative increase in the total power loss (wave shadow) moving from the 1-WEC (upper panels) and 3-WEC (middle panels) to the 5-WEC (lower panels) configurations. Thus, there is also an inherently corresponding increase in the signal-to-noise ratio of the power loss estimates with the increased number of WECs. For the regular wave cases (left column), there is an evident peak in the SWAN-simulated power loss around $T = 1.5$ s, which mimics the RCW curve that was used (see Fig. 3), as expected, and is independently confirmed from the observed wave shadow data here (also see Fig. 4).

We also note that the SWAN data comparisons for regular wave conditions need to be considered with care, especially for cases involving regular waves with short periods, because of the difficulties involved in using point observations to quantify the spatially, highly variable wave field either offshore or in the lee of the WECs (see Fig. 4). There is evidence of increased observed power loss at periods shorter than about 1.4 s (the peak of the RCW curve). However, the WAMIT results discussed in “[WAMIT-data comparisons](#)” suggest that reflected and radiated waves might play an increased role for these shorter periods, so that the power loss observed in the lee of the WECs cannot entirely be attributed to power absorption. Instead, wave power has been spatially redistributed. Given the reliance on only wave absorption information (via the RCW curve), the SWAN model cannot reproduce these more complex power redistribution effects.

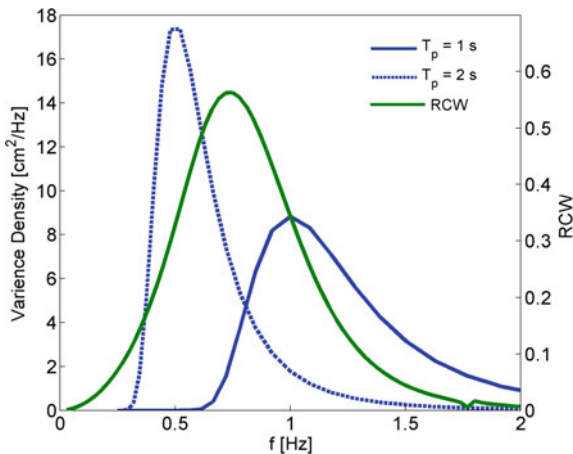
There are also SWAN data discrepancies in the regular wave cases (left column) that involve periods longer than about 2 s. For these long-period cases, the SWAN simulations indicate no energy loss (or gain), but the observations suggest some energy gain. Again, the SWAN simulations correctly conform to the experimental RCW curve, and the SWAN data difference likely derives from the offshore wave scattering from the WECs. Specifically, if the majority of gages in the offshore array happened to be located in a valley of the partial standing wave pattern (see Fig. 6, left-bottom panel) and the lee array located in a lower amplitude wave shadow, as expected, the wave height differences between the observational arrays would lead to a negative power deficit (i.e., power gain).

Discussion

Next, we show results from simulations using the two models, explicitly keeping the model WEC power capture characteristics the same in both, so that we can illustrate how the scattering and radiation affect the ability of the SWAN model (with the associated WEC parameterization) to simulate the wave shadow. The results also demonstrate the impact of the scattering and radiated fields on the severity of the wave shadow, which has implications for the overall nearshore wave effects of WEC arrays.

The simulation conditions bookmark the range of scattering behavior seen in both the model and experimental results in the previous section. In particular, model results are obtained for two regular wave cases with $T = 1$ and $T = 2$ s and four

Fig. 8 Wave spectra (1-second peak period in solid blue and 2-second period in dashed blue) and WAMIT-computed RCW (green line, also shown in Fig. 3)



spectral seas cases—unidirectional waves and directionally spread seas both with $T_p = 1$ and $T_p = 2$ s. As can be seen in Fig. 8, the two wave periods chosen have nearly the same model RCW value of ~ 0.35 . This enables a comparison of their differing scattered and radiated wave fields in a setting where the expected power capture is the same. All simulations have the same incident wave height, but the two different spectral peak periods have somewhat different spectral shapes that follow the Pierson–Moskowitz model (also shown in Fig. 8). Directional spreading (two cases) used a \cos^{2s} distribution with a spreading parameter of $s = 10$.

All SWAN runs were carried out with and without the diffraction option, except for the regular wave $T = 2$ s case where convergence could not be attained for SWAN with diffraction (see missing panel in Fig. 9). To allow for a more direct comparison, the power capture characteristics are kept the same in both models by using the RCW performance curve computed by WAMIT (shown in Figs. 3 and 8) for the SWAN simulations.

To assess the utility of SWAN in estimating the wave shadow, we begin by analyzing the simulations involving regular waves (see top two rows in Fig. 9). Because the WEC model in SWAN is based solely on energy extraction, the SWAN results (with no diffraction effects) for both periods are identical. For these cases, the wave shadow produced by SWAN extends onshore as a narrow streak, and there is almost no recovery in wave height with distance to the lee of the WEC. In contrast, the WAMIT wave fields for the two periods are quite different from one another. The scattered and radiated wave components are more energetic for the shorter period case, as evidenced by the stronger standing wave ridge patterns. Because these scattering processes redistribute the wave energy spatially, the wave shadow is also clearly more pronounced for the shorter period case, even though the amount of energy extracted from the wave field is similar for both periods. When the diffraction option in SWAN is used, the shadow spreads alongshore more readily, as expected, and the resulting shadow region is little more similar to the

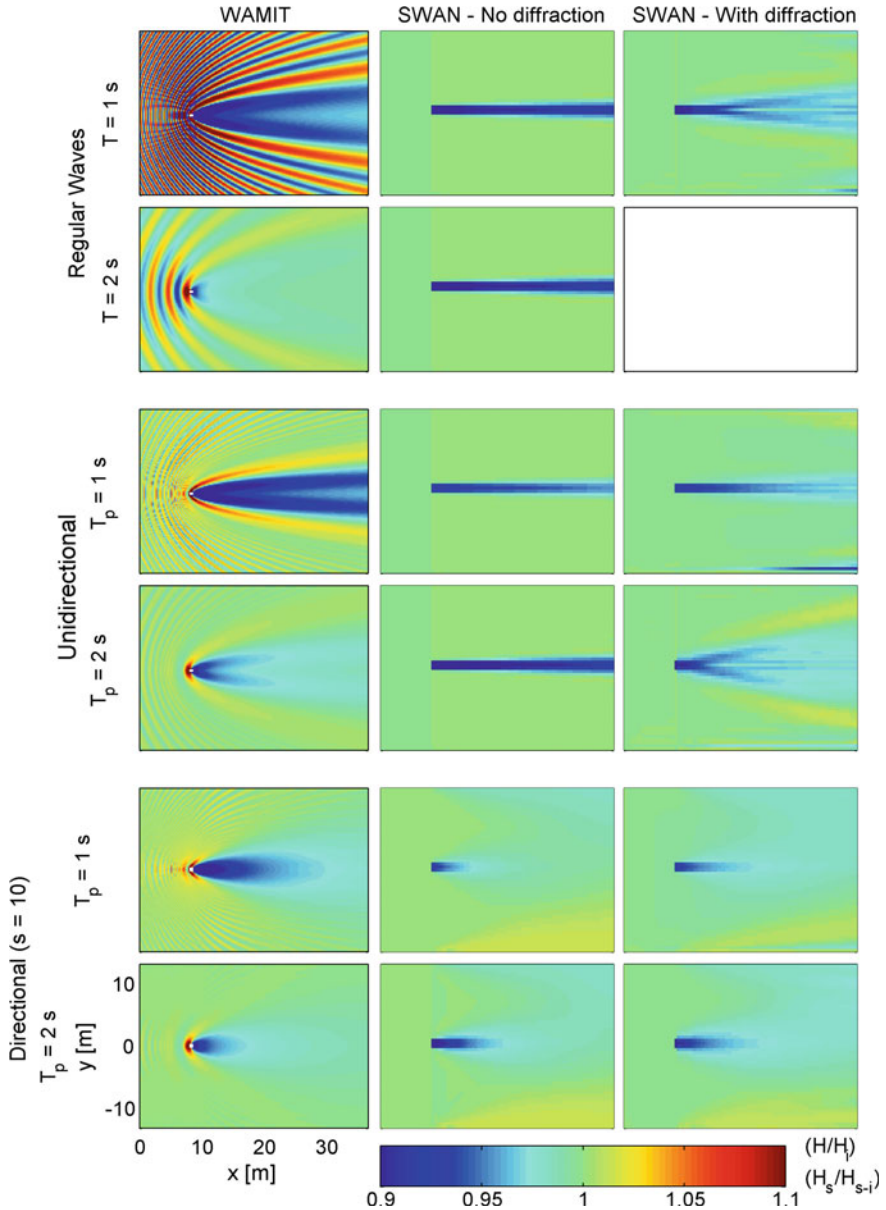


Fig. 9 WAMIT-SWAN wave field comparisons for regular waves (rows 1 and 2), unidirectional random waves (rows 3 and 4), and directionally spread random waves (rows 5 and 6). Each type has both 1-second and 2-second peak periods. The SWAN solution did not converge for $T = 2\text{ s}$ regular waves w/diffraction

WAMIT results. However, the spatial variability related to the scattered and radiated waves is not reproduced.

In the previous section, we noted from Fig. 7 that the SWAN model consistently underestimated the observed wave shadow magnitude for regular wave conditions from 1.0 to 1.4 s, i.e., for waves with smaller periods than those of the peak (experimental) RCW. This under-prediction occurs because the wave shadow associated with these shorter period waves is only partially controlled by the amount of wave energy absorption by the WEC; it is also affected by the increased wave-scattering processes at these wave periods. Note that Beels et al. (2010) observed a similar phenomenon in their modeling of the Wave Dragon WEC. Specifically, they noted that the wave height reduction behind the device could not always be explained by energy absorption; it could instead be related to wave reflection. This is also supported by the WAMIT results in Fig. 9, which shows that the short-period cases consistently have a greater wave shadow magnitude than the longer period cases (for both regular and spectral sea states).

For wave periods around the RCW peak, the wave energy flux deficit shown in Fig. 7 indicates that the SWAN model could better represent the observed wave shadow. This is because at these periods, the wave shadow is most closely linked to the absorbed power. For even longer periods, for which the RCW is near zero, the experimental shadow observations are again dominated by the redistribution due to scattering processes, and the SWAN simulations do not produce wave shadows because there is no expected power capture at those wave periods.

For the unidirectional sea simulations (Fig. 9 middle panels), the shorter period WAMIT results display more spatial variability, a more pronounced shadow region, and a distinct wave amplification region in the shape of a parabola around the wave shadow. Similar to its performance in the regular wave cases, the SWAN model is not able to capture any of these features. In the WAMIT simulation, the wave height modification is less pronounced for the longer period case, and the standing wave ridge pattern offshore is almost absent. This is again due to the reduced scattering and radiation and also to the smoothing induced by the phase relationships between the set of wave periods present. Here, SWAN, considering spectral wave conditions and with the diffraction option, is better able to reproduce the wave height variability in the lee of the WEC as compared to SWAN performance in the regular wave case.

WAMIT results associated with the directionally spread seas results (bottom two rows in Fig. 9) show a much smoother wave height modification pattern, as would be expected in the presence of wave components from a variety of directions. Here, the results from the different periods are more similar, though the amplitude of the wave shadow is still larger for the short-period case. The effect of the diffraction option in the SWAN model is less important here, which is an expected result for directionally spread waves. Overall, the SWAN results for the longer peak period most closely resemble the WAMIT wave field, but only in the lee of the device. In general, the SWAN results for the directionally spread cases are a better match to the WAMIT results than those for either the unidirectional or regular wave cases.

Conclusions

In this chapter, we have presented results from a laboratory experiment conducted using an array of 1:33 scale WEC devices to ascertain the wave field modifications caused by the presence of the WECs. Further, two commonly used numerical models—the phase-resolving model WAMIT and the phase-averaged model SWAN—were applied to the conditions of the experiment and validated using the available observations. The SWAN simulations took into account the frequency-dependent nature of the wave energy absorption through a nested domain approach, whereby the spectra at the locations of the devices were altered based on preexisting knowledge of the power absorption curve leading to the simulated wave field modifications in the lee of the devices.

We found that the short-scale variability predicted by phase-resolving models such as WAMIT is indeed consistent with the observations from an array of wave gages both offshore and in the lee of the WECs. The short-scale variability is linked to a standing wave ridge pattern that arises because of wave scattering by the WEC device. The scattered waves are generated by scattering from the device and radiated waves generated by device motion. At short-wave periods, this high short-scale wave height variability complicates the interpretation of point observations. The issues arise either because the variability cannot be adequately resolved, or the observations are biased toward either ridges or valleys in the partial standing wave pattern.

Overall, the results indicate two things: First, the WEC parameterization we have used in the SWAN model can be effective at simulating the wave shadows induced by WEC arrays under conditions where the wave shadow is primarily controlled by the WEC power capture characteristics rather than by the redistribution of wave energy due to scattering and radiation. Generally speaking, these conditions occur when much of the wave energy lies at wave periods around the RCW peak period and higher when the RCW is still nonzero. The parameterization will underestimate the wave shadow when the significant energy lies below the RCW peak period, where scattering and radiation are of increased importance. The parameterization does not capture the partial standing wave field offshore of WEC arrays because it is caused by scattering and radiation and not power capture.

Second, the analysis of wave shadows induced by WECs using the WAMIT simulations has indicated that under similar power capture characteristics, it is possible to have significantly different wave shadows. Specifically, the WAMIT results demonstrate that the shorter period cases have shadows of larger magnitude and more complicated offshore structure, even when frequency and directional spreading are included. It is reasonable to argue that a characteristic potential environmental effect of WEC arrays is the amount of wave field modification induced by the presence of an array. Hence, these results indicate that even when the potential for wave energy capture is normalized for (i.e., similar power capture conditions), the environmental effects of WEC arrays (i.e., the wave shadow) are

reduced when WECs are designed to operate such that the expected wave climate lies on the longer period side of the WEC RCW curve.

Acknowledgements This work was supported by the US Department of Energy (Award #DE-EE0002658), Sandia National Laboratories, and Columbia Power Technologies under Research Subagreement NO. 2010-1698. Additional support came from the Oregon Wave Energy Trust through Award Number OIC-0911-109. We also wish to thank Ken Rhinefrank, Joe Prudell, Al Schacher, Erik Hammagren, Tim Maddux, and the staff of the Hinsdale Wave Research Laboratory for their help in the experimental effort.

References

- Abanades, J., Greaves, D., & Iglesias, G. (2014a). Wave farm impact on the beach profile: A case study. *Coastal Engineering*, *86*, 36–44.
- Abanades, J., Greaves, D., & Iglesias, G. (2014b). Coastal defence through wave farms. *Coastal Engineering*, *91*, 299–307.
- Alexandre, A., Stallard, T., & Stansby, P. K. (2009). Transformation of wave spectra across a line of wave devices. *Proceedings of the 8th European Wave and Tidal Energy Conference (EWTEC 2009)*.
- Ashton, I. G. C., Johanning, L., & Linfoot, B. (2009). Measurement of the effect of power absorption in the lee of a wave energy converter. *Proceedings of OMAE 2009*, OMAE2009–79793.
- Babarit, A., Hals, J., Muliawan, M. J., Kurniawan, A., Moan, T., & Krokstad, J. (2012). Numerical benchmarking study of a selection of wave energy converters. *Renewable Energy*, *41*, 44–63.
- Babarit, A. (2013). On the park effect in arrays of oscillating wave energy converters. *Renewable Energy*, *58*, 68–78.
- Beels, C., Troch, P., De Visch, K., Kofoed, J. P., & De Backer, G. (2010). Application of the time-dependent mild-slope equations for the simulation of wake effects in the lee of a farm of wave dragon wave energy converters. *Renewable Energy*, *35*, 1644–1661.
- Black, C., & Haller, M. C. (2013). *Analysis of waves in the near-field of wave energy converter arrays through stereo video*, Abstract: OS11C-1657. San Francisco, CA: AGU Fall Meeting.
- Booij, N., Ris, R. C., & Holthuijsen, L. H. (1999). A third-generation wave model for coastal regions—1. Model description and validation. *Journal Geophysical Research*, *104*(C4), 7649–7666.
- Borgarino, B., Babarit, A., & Ferrant, P. (2012). Impact of wave interactions effects on energy absorption in large arrays of wave energy converters. *Ocean Engineering*, *41*, 79–88.
- Chang, G., Ruehl, K., Jones, C. A., Roberts, J., & Chartrand, C. (2016). Numerical modeling of the effects of wave energy converter characteristics on nearshore wave conditions. *Renewable Energy*, *89*, 636–648.
- Chatjigeorgiou, I. K. (2011). Three dimensional wave scattering by arrays of elliptical and circular cylinders. *Ocean Engineering*, *38*, 1480–1494.
- Choi, J., Lim, C. H., Lee, J. I. & Yoon S. B. (2009). Evolution of waves and currents over a submerged laboratory shoal. *Coastal Engineering*, Vol. 56, 297–312.
- Day, A. H., Babarit, A., Fontaine, A., He, Y.-P., Kraskowski, M., Mirai, M., et al. (2015). *Ocean Engineering*, *108*, 46–69.
- De Andrés, A. D., Guanche, R., Meneses, L., Vidal, C., & Losada, I. J. (2014). Factors that influence array layout on wave energy farms. *Ocean Engineering*, *82*, 32–41.
- Eriksson, M., Waters, R., Svensson, O., Isberg, J., & Leijon, M. (2007). Wave power absorption: Experiments in open sea and simulation. *Journal of Applied Physics*, *102*, 084910.

- de Falcão, A. F. (2010). O., Wave energy utilization: A review of technologies. *Renewable and Sustainable Energy Reviews*, 14, 899–918.
- Farley, F. J. M., (2011). Far-field theory of wave power capture by oscillating systems. *Philosophical Transactions of the Royal Society A: Mathematical, Physical and Engineering Sciences*, 370(1959), 278–287.
- Fernandez, H., Iglesias, G., Carballo, R., Castro, A., Fraguera, J. A., Taveira-Pinto, F., et al. (2012). The new wave energy converter WaveCat: Concept and laboratory tests. *Marine Structures*, 29, 58–70.
- Flocard, F., & Finnigan, T. D. (2010). Laboratory experiments on the power capture of pitching vertical cylinders in waves. *Ocean Engineering*, 37, 989–997.
- Folley, M., & Whittaker, T. (2013). Validating a spectral-domain model of an OWC using physical model data. *International Journal of Marine Energy*, 2, 1–11.
- Gonzalez-Santamaria, R., Zou, Q. P., & Pan, S. (2013). Impacts of a wave farm on waves, currents and coastal morphology in Southeast England. *Estuaries and Coasts*, 1, 1–14.
- Haller, M. C., Porter, A., Lenee-Bluhm, P., Rhinefrank, K., Hammagren, E., Özkan-Haller, T. & Newborn, D. (2011). Laboratory observations of waves in the vicinity of WEC-arrays. *Proceedings of European Wave and Tidal Energy Conference (EWTEC 2011)*, Paper No. 419.
- Holthuijsen, L., Herman, A. & Booij, N. (2003). Phase-decoupled refraction–diffraction for spectral wave models. *Coastal Engineering*, 49(4), 291–305.
- Ilic, S., van der Westhuysen, A. J., Roelvink, J. A., & Chadwick, A. J. (2007). Multidirectional wave transformation around detached breakwaters. *Coastal Engineering*, 54, 775–789.
- Iturrioz, A., Guanche, R., Armesto, J. A., Alves, M. A., Vidal, C., & Losada, I. J. (2014). Time-domain modeling of a fixed detached oscillating water column towards a floating multi-chamber device. *Ocean Engineering*, 76, 65–74.
- Kara, F. (2016). Time domain prediction of power absorption from ocean waves with wave energy converter arrays. *Renewable Energy*, 92, 30–46.
- Li, Y., & Yu, Y.-H. (2012). A synthesis of numerical methods for modeling wave energy converter-point absorbers. *Renewable and Sustainable Energy Reviews*, 16, 4352–4364.
- McNatt, J. C., Venugopal, V., & Forehand, D. (2013). The cylindrical wave field of wave energy converters. *International Journal of Marine Energy*, 3–4, e26–e39.
- Mei, C. C. (2012). Hydrodynamic principles of wave power extraction. *Philosophical Transactions of the Royal Society A*, 370, 208–234.
- Mendoza, E., Silva, R., Zanuttigh, B., Angelelli, E., Andersen, T. L., Martinelli, L., et al. (2014). Beach response to wave energy converter farms acting as coastal defence. *Coastal Engineering*, 87, 97–111.
- Millar, D. L., Smith, H. C. M., & Reeve, D. E. (2007). Modelling analysis of the sensitivity of shoreline change to a wave farm. *Ocean Engineering*, 34(5–6), 884–901.
- Nihous, G. C. (2012). Wave power extraction by arbitrary arrays of non-diffracting oscillating water columns. *Ocean Engineering*, 51, 94–105.
- O’Dea, A., Haller, M. C. & Özkan-Haller, H. T. (2015). The impact of wave energy converter arrays on wave-induced forcing in the surf zone. *Submitted to Renewable Energy*.
- Palha, A., Mendes, L., Fortes, C. J., Brito-Melo, A., & Sarmiento, A. (2010). The impact of wave energy farms in the shoreline wave climate: Portuguese pilot zone case study using Pelamis energy wave devices. *Renewable Energy*, 35(1), 62–77.
- Payne, G. S., Taylor, J. R. M., Bruce, T., & Parkin, P. (2008). Assessment of boundary-element method for modelling a free-floating sloped wave energy device. Part 2: Experimental validation. *Ocean Engineering*, 35, 342–357.
- Porter, A. K., Haller, M. C. & Lenee-Bluhm, P. (2012). Laboratory observations and numerical modeling of the effects of an array of wave energy converters. *Proceedings of 33rd ICCE 2012*. Santander, Spain, doi:10.9753/icce.v33.management.67.
- Rhinefrank, K., et al. (2013). Benchmark Modeling of the Near-Field and Far-Field Wave Effects of Wave Energy Arrays, *Columbia Power Technologies Final Report*, DE-EE0002658, U.S. Dept. of Energy, www.osti.gov/servlets/purl/1060889/.

- Rusu, E., & Guedes, C. (2013). Soares, Coastal impact induced by a Pelamis wave farm operating in the Portuguese nearshore. *Renewable Energy*, 58, 34–49.
- Silverthorne, K. E. & Folley, M. (2013). A new numerical representation of wave energy converters in a spectral wave model. *Proceedings of the 10th European Wave and Tidal Energy Conference (EWTEC 2013)*.
- Sinha, A., Karmakar, D., & GuedesSoares, C. (2016). Performance of optimally tuned arrays of heaving point absorbers. *Renewable Energy*, 92, 517–531.
- Smith, H. C. M., Pearce, C., & Millar, D. L. (2012). Further analysis of change in nearshore wave climate due to an offshore wave farm: an enhanced case study for the Wave Hub site. *Renewable Energy*, 40(1), 51–64.
- Stratigaki, V., Troch, P., Stallard, T., Forehand, D., Folley, M., Kofoed, J. P., et al. (2015). Sea-state modification and heaving float interaction factors from physical modelling of arrays of wave energy converters. *Journal of Renewable and Sustainable Energy*, 7, 061705.
- Tutar, M., & Veci, I. (2016). Performance analysis of a horizontal axis 3-bladed Savonius type wave turbine in an experimental wave flume (EWF). *Renewable Energy*, 86, 8–25.
- WAMIT, Inc., (2000). WAMIT user manual version 6.0, 6.0PC, 5.3S. Available from www.wamit.com.
- Waters, R., et al. (2007). Experimental results from sea trials of an offshore wave energy system. *Applied Physics Letters*, 90, 034105.
- Waters, R., et al. (2011). Ocean wave energy absorption in response to wave period and amplitude —Offshore experiments on a wave energy converter. *IET Renewable Power Generation*, 5(6), 465–469.
- Weller, S. D., Stallard, T. J. & Stansby, P. K. (2010). Experimental measurements of irregular wave interaction factors in closely spaced arrays. *IET Renewable Power Generation*, 4(6), 628–637.
- Zijlema, M. (2010). Computation of wind-wave spectra in coastal waters with SWAN on unstructured grids. *Coastal Engineering*, 57(3), 267–277.